

PCCP

Accepted Manuscript



This is an *Accepted Manuscript*, which has been through the Royal Society of Chemistry peer review process and has been accepted for publication.

Accepted Manuscripts are published online shortly after acceptance, before technical editing, formatting and proof reading. Using this free service, authors can make their results available to the community, in citable form, before we publish the edited article. We will replace this *Accepted Manuscript* with the edited and formatted *Advance Article* as soon as it is available.

You can find more information about *Accepted Manuscripts* in the [Information for Authors](#).

Please note that technical editing may introduce minor changes to the text and/or graphics, which may alter content. The journal's standard [Terms & Conditions](#) and the [Ethical guidelines](#) still apply. In no event shall the Royal Society of Chemistry be held responsible for any errors or omissions in this *Accepted Manuscript* or any consequences arising from the use of any information it contains.



PCCP

ARTICLE

Structural Variety beyond Appearance: High-pressure Phases of CrB₄ in comparison with FeB₄

Received 00th January 20xx,
Accepted 00th January 20xx

DOI: 10.1039/x0xx00000x

www.rsc.org/

Yunkun Zhang,^a Lailei Wu,^{*a} Biao Wan,^a Yan Zhao,^a Rui Gao,^b Zhiping Li,^b Jingwu Zhang^{*a},
Huiyang Gou^{*cd} and Ho-kwang Mao^{cd}

Employing Particle Swarm Optimization (PSO) combined with first-principles calculations, we systemically studied high-pressure behaviors of hard CrB₄. Our predictions reveal a distinct structural evolution under pressure for CrB₄ despite having the same initial structure with FeB₄. CrB₄ is found to adopt a new *P2/m* structure above 196 GPa, another *Pm* structure at a pressure range of 261-294 GPa and then a *Pmma* structure beyond 294 GPa. Instead of puckering boron sheets in initial structure, the high-pressure phases have the planar boron sheets with different motifs upon compression. Comparatively, FeB₄ prefers an *I4₁/acd* structure over 48 GPa with tetrahedron B₄ units and a *P2₁3* structure above 231 GPa having equilateral triangle B₃ units. Significantly, CrB₄ exhibits the persistent metallic behaviors in contrast with the semiconducting features of FeB₄ upon compression. The varied pressure response of hard tetraborides studied here is of importance for understanding boron-rich compounds and designing new materials with superlative properties.

I. Introduction

Transition metal (TM) borides have continued to attract much attention over decades because of great potentials for the development of next generation hard/superhard materials.¹⁻⁷ The synthesis of 5*d* noble metal borides, e.g. OsB₂⁴ and ReB₂³, was expected to yield superhard materials due to the strong covalent interactions between TM-B and B-B. Although great efforts have been made to obtain the high bulk modulus in these borides, however, this incompressibility did not guarantee the better mechanical properties,⁷ e.g. hardness. The continuing searching for

possible superhard materials is thus focusing on the more boron-rich compounds.⁸⁻¹¹ Once more boron atoms are introduced into the metal lattices, the mechanical properties are expected to be enhanced due to the presence of three-dimensional (3D) boron networks, e. g. nominal WB₄.¹²⁻¹⁴ In comparison with 5*d* metal borides, the weak bonding between metal and boron in 3*d* metal borides makes them less attractive for potentially hard materials. Nevertheless, the studies of 3*d* transition metal tetraborides (TMB₄), CrB₄^{8,15,16}, FeB₄^{9,17} and MnB₄^{10,11,18}, have become one of the exciting topics because of the possible higher hardness, together with intriguing physical properties, such as superconductivity, semiconductivity and magnetism. For example, *Pnmm* type FeB₄ was predicted and experimentally confirmed to be phonon mediated superconductor.^{9,15} MnB₄ opens a band gap at Fermi level due to the Peierls distortion of Mn chains in the monoclinic symmetry.^{10,11,18} Additionally, they also show the incompressible behavior due to the presence of short boron-boron bonds in the boron networks, comparable to 5*d* metal borides. The unique features of 3*d* TMB₄ are inspiring for a variety of engineering applications.

^aKey Laboratory of Metastable Materials Science and Technology, College of Material Science and Engineering, Yanshan University, Qinhuangdao 066004, China.

^bKey Laboratory of Applied Chemistry, College of Environmental and Chemical Engineering, Yanshan University, Qinhuangdao 066004, China.

^cCenter for High Pressure Science and Technology Advanced Research, Shanghai 201203, China

^dGeophysical Laboratory, Carnegie Institution of Washington, 5251 Broad Branch Road NW, Washington, DC 20015, USA

Correspondence and requests for materials should be addressed to H. Gou (huiyang.gou@gmail.com), L. Wu (wll@ysu.edu.cn) and J. Zhang (zjw@ysu.edu.cn)

†Electronic Supplementary Information (ESI) available: [details of any supplementary information available should be included here]. See DOI: 10.1039/x0xx00000x

Studies of material behaviors under pressure are of great importance for both planetary physics and materials science. Application of pressure greatly stimulated the discovery of the unexpected structural materials, e.g. NaCl_3 and Na_3Cl ,¹⁹ and physical phenomena, e.g. metal-insulator transitions in Li ²⁰ and Na ²¹. In these studies, structural prediction strategies have showed the great ability to assist and even guide the material discovery in experiments.²²⁻²⁴ The improvement of density functional theory-based methods and the development of computational resources predict complex configurations given only the composition, leading to identification of exotic high-pressure (HP) phases.^{25, 26} Recently, Kotmool et al.²⁷ theoretically proposed a structure change of FeB_4 from superconductor to semiconductor above 53.7 GPa. This phase is found to be stable up to 300 GPa. Under further compression, another phase transition above 695 GPa was reported by Jiang et al.²⁸ This new cubic $Im\bar{3}m$ phase was predicted to be stable up to 1TPa. As we know, the neighboring CrB_4 have similar structural and metallic features at ambient condition. However, there is little information about high-pressure behaviors of CrB_4 . Here we comparatively explored the HP phases of CrB_4 and FeB_4 within structure search methodology. Furthermore, we have studied their structures, mechanical and electronic features through the first-principles calculations. Our predictions are expected to greatly stimulate future experiments to synthesize these phases.

II. Methods

Structure searches at high pressure (50, 100, 200 and 300 GPa) of CrB_4 and FeB_4 within six formula units were performed by the particle swarm optimization methodology as implemented in the CALYPSO code.^{25, 26} CASTEP code was used for the structural optimizations and energy calculations for various structures.²⁹ Exchange and correlation functional was treated by generalized gradient approximation with Perdew-Burke-Ernzerhof (GGA-PBE).³⁰ An energy cut-off of 500 eV for the plane-wave basis, and a dense k -point grid in the Monkhorst-Pack scheme for integration in Brillouin zone were tested to ensure the convergence of the total energy to within 1 meV per formula unit. By calculating the elastic constants of crystals, C_{ij} , bulk modulus, B , and shear modulus, G , of each structure were obtained using the Voight-Reuss-Hill (VRH) approximation.³¹ The phonon spectrums of HP phases of CrB_4 and FeB_4 have been calculated by finite displacement methods to examine their dynamical stabilities. The structures were visualized by VESTA.³²

III. Results and discussion

The structure searches produced a large variety of candidates for high pressure phases, and the enthalpy difference under compression for CrB_4 and FeB_4 are summarized in Fig. 1. To make a complete comparison, the previously proposed $Im\bar{3}m$ phase was also added for

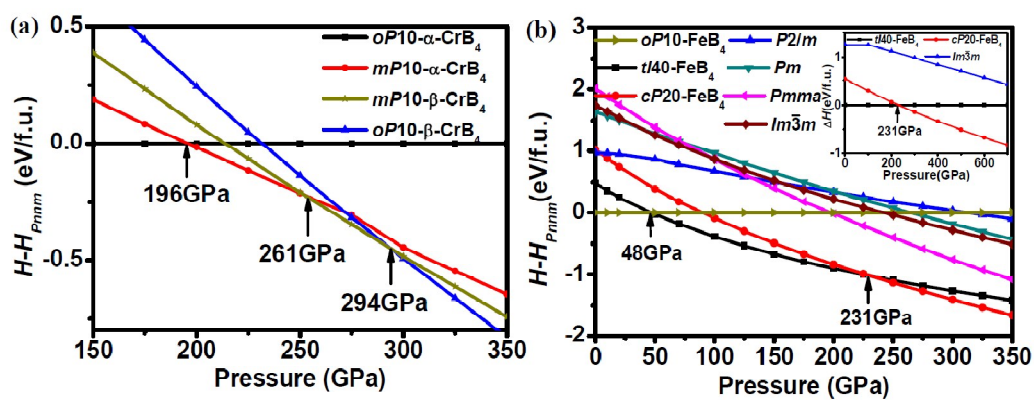
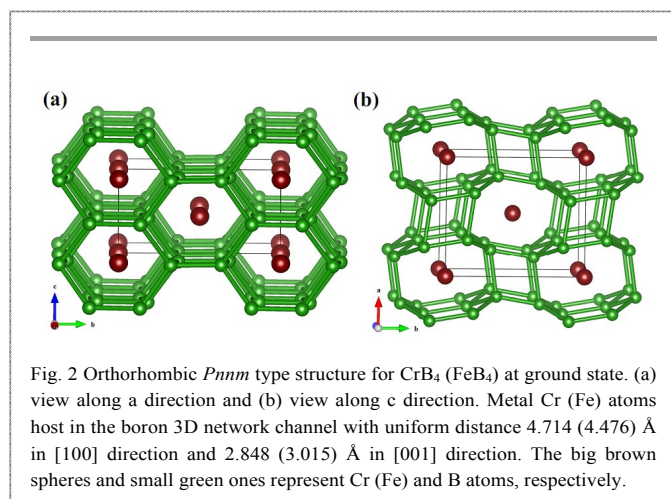


Fig. 1 Enthalpy difference (relative to $Pnmm$ structure) as a function of pressure for CrB_4 (a) and FeB_4 (b) phases. Formation enthalpies of $cP20\text{-FeB}_4$ and $Im\bar{3}m\text{-FeB}_4$ relative to $tI40\text{-FeB}_4$ are given in the inset.

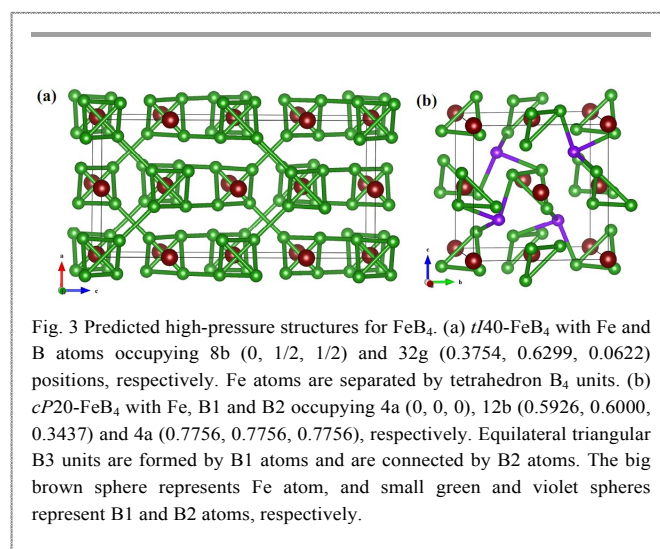
FeB₄.²⁸ The total energy as a function of unit volume (per f.u.) curves for CrB₄ and FeB₄ are shown in Fig. S1 of the Supplementary Information (SI).

As shown in Fig. 1 and S1, the structure searches confirmed the orthorhombic *Pnmm* structure for CrB₄ and FeB₄ at ground state (Space group (SG) No. 58, denoted as *oP10-α*-CrB₄ and *oP10*-FeB₄ later).^{8,9} In the orthorhombic structure (Fig. 2), the boron atoms are connected by the buckling layers with six-member rings in *yz* crystallographic plane, the neighboring boron layers are linked together by B₄ rhomboid units to form a 3D boron network. The metal Cr (Fe) atoms are situated in the boron channels with uniform bond distance of 4.714 Å (4.476 Å for FeB₄) in [100] direction, and 2.848 Å (3.015 Å for FeB₄) in [001] direction. Upon compression, a tetragonal *I4₁/acd* type FeB₄ (SG No. 142, denoted as *tI40*-FeB₄ shown in Fig. 3(a)) is energetically preferable above 48 GPa (Fig. 1(b)), in agreement with previously predictions, 53.7 GPa by Kotmool et al.²⁷ and 55.0 GPa by Jiang et al.²⁸ Intriguingly, a B₄ tetrahedron appeared in *tI40*-FeB₄ differs from the planar rhomboid B₄ arrangement in *oP10*-FeB₄. In this configuration, a diverse 3D boron network is found with varied bond distances, four B-B bonds with a distance of 1.818 Å and two B-B bonds with a distance of 1.842 Å, all of the tetrahedrons are closely connected with vertexes of other four tetrahedrons by a B-B bond distance of 1.813 Å. Similar B₄ tetrahedrons were also found in B₄Cl₄.³³ Besides, *tI40*-FeB₄ resembles a NaCl-type structure by 1×1×2 supercell, with the B₄ tetrahedrons and Fe atoms playing the roles of ‘anions’ and ‘cations’, respectively. The Fe atoms in *tI40*-FeB₄ occupied all the



octahedral voids constructed by six B₄ tetrahedrons, and each Fe atom has twelve neighboring Fe atoms with a uniform distance of 3.612 Å. Under further compression, however, we discovered a new cubic *P2₁3*-type FeB₄ (SG No. 198, denoted as *cP20*-FeB₄ hereafter), which is thermodynamically more favorable than any other phases above 231 GPa (see Fig. 1(b)). Certainly, *cP20*-FeB₄ is superior to previously hypothetical *Im3m* phase²⁸ over a wide pressure up to 700 GPa. The formation enthalpy is much lower than that of *Im3m* phase by about 1.08 eV/f.u. at 231 GPa (as shown in Fig. 1(b)). In *cP20*-FeB₄ as shown in Fig. 3(b), B1 atoms form B₃ equilateral triangle (ET-B₃) by B1-B1 bonds of 1.819 Å, and the ET-B₃ was connected together through B2 atoms by B1-B2 bonds of 1.848 Å. The *cP20*-FeB₄ structure can be viewed as a modified NaCl-type structure, with ET-B₃ units and Fe atoms playing the roles of ‘anions’ and ‘cations’, respectively, and B2 atoms occupying half of the tetrahedral sites. The distance between neighboring Fe atoms is 3.602 Å, shorter than that in *tI40*-FeB₄.

The success in HP phases for FeB₄ makes us confidently move on to CrB₄. Initially, CrB₄ was expected to have the same pathway due to the similarity of ground state structure. As shown in Fig. S2, however, both *P2₁3*-type and *I4₁/acd*-type structure are energetically unfavorable in the whole considered pressure range. *oP10-α*-CrB₄ is persistent up to 196 GPa and transforms into a monoclinic *P2₁/m* type CrB₄ (SG No. 10, denoted as *mP10-α*-CrB₄ hereafter). At about 261 GPa, another monoclinic *Pm* phase (SG No. 6, denoted as *mP10-β*-CrB₄ hereafter) appears with a lower formation enthalpy, and then it



is energetically substituted by an orthorhombic *Pmma* type structure (SG No. 51, denoted as *oP10*- β -CrB₄ hereafter), the latter is thermodynamic stable at least up to 350 GPa. Rather than the distinctive 3D boron networks of FeB₄ phases, all of high pressure structures of CrB₄ are closely packed by the sequence of ABAB... along the [010] direction (see Fig. 4). A is planar boron sheet; B is metal Cr-layer inserted by boron atoms. Generally, such a planar boron network usually introduces metallic features because the *sp*- or *sp*²-hybridized orbitals form a network of σ bonds, and the non-filled *p*_z orbital form delocalized π bonds (Detailed electronic analysis are presented later). The major differences among these phases stem from the motifs of planar boron sheets and varied B-B distances within Cr-B layers. For *mP10*- α -CrB₄, the planar boron

sheets are composed of rhomboid B₆ (or conjugated rhomboid B₄) units with interior B-B bonds of 1.728 Å -1.785 Å. Rhomboid B₆ units are vertex connected together by the B-B distances of 1.799 Å and 1.935 Å, and the interesting B₁₀ rings are formed. Simultaneously, B₂ pairs with a bond length of 1.727 Å appear within Cr-B layer, the neighboring boron pairs are separated by a distance of 3.889 Å along *a* direction. For *mP10*- β -CrB₄, the conjugated rhomboid B₄ units are separated, and the planar B₆ and B₈ rings are showed up. The B-B bond length in the boron sheets varies from 1.694 Å to 1.837 Å, slightly shorter than those in *mP10*- α phase. Interestingly, boron distance in B₂ pairs enlarges to 1.782 Å and the separation between boron pairs shortens to 3.678 Å along *a* direction in comparison with *mP10*- α phase. When goes to *oP10*- β -

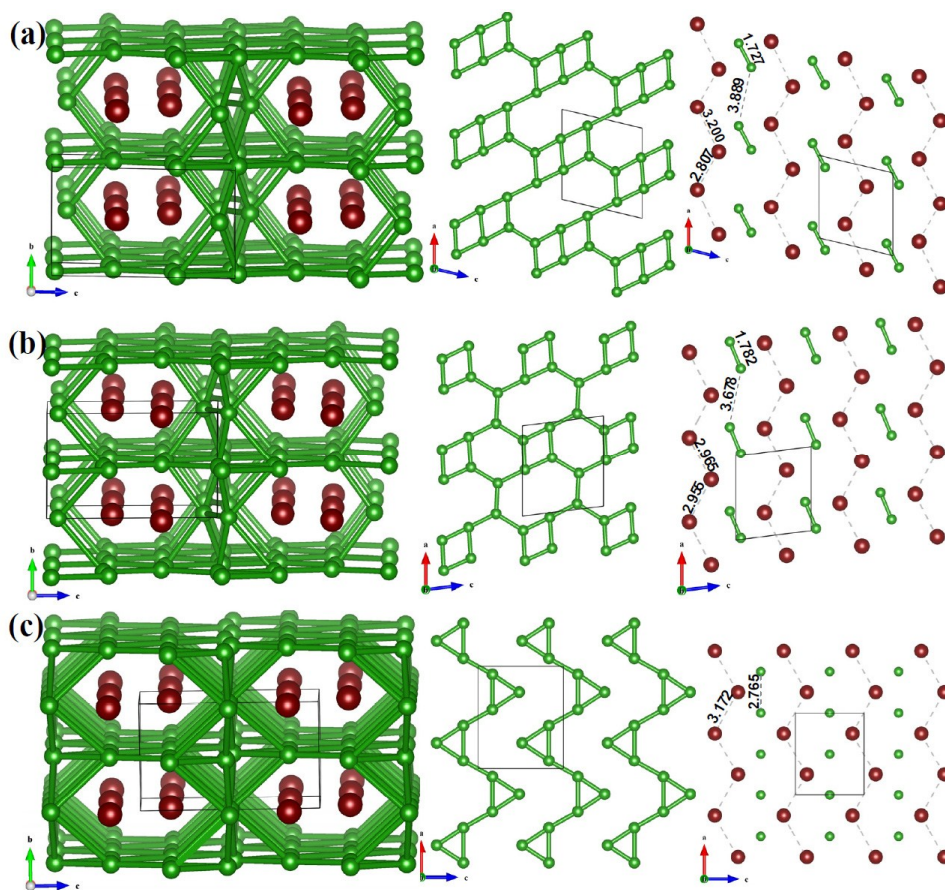


Fig. 4 Predicted high-pressure phase structures for CrB₄. (a) *mP10*- α -CrB₄ with atomic coordinates Cr [2n, (0.2404, 1/2, 0.3549)], B [2m, (0.5523, 0, 0.3374)], [2m, (0.6687, 0, 0.9824)], [2m (0.1178, 0, 0.6829)] and [2n (0.8745, 1/2, 0.0846)]; (b) *mP10*- β -CrB₄ with atomic coordinates Cr [1a (0.7467, 0, 0.6748)] and [1a, (0.2796, 0, 0.3836)]; B [1a, (0.0167, 0, 0.0671)], [1a, (0.3456, 0, 0.9210)], [1b, (0.6063, 1/2, 0.3654)], [1b, (0.0621, 1/2, 0.6728)], [1b, (0.3951, 1/2, 0.6950)], [1b, (0.9479, 1/2, 0.3346)], [1b, (0.5075, 1/2, 0.0303)] and [1b, (0.8417, 1/2, 0.0080)]; (c) *oP10*- β -CrB₄ with atomic coordinates Cr [2e, (1/4, 0, 0.1687)]; B [2f, (1/4, 1/2, 0.5180)], [2c, (0, 0, 1/2)] and [4j, (0.4214, 1/2, 0.8302)]. Planar boron sheets and zigzag Cr-Cr chains are typical characteristics. The big brown and the small green spheres represent Cr and B atoms, respectively.

CrB₄ phase, the rhomboid B₄ units are replaced by vertex connected B₃ triangles with two B-B bonds of 1.724 Å and one B-B bond of 1.896 Å, the B-B bonds between the neighboring B₃ units are 1.791 Å. Additionally, the B₂ pairs in Cr layers are also separated with a uniform distance of 2.765 Å. In three HP phases, the planar boron sheets are connected by boron pairs (or isolated boron atoms) with B-B bonds of 1.788 and 1.807 Å for *mP10-α*-CrB₄, 1.752-1.918 Å for *mP10-β*-CrB₄, and 1.949 Å and 2.095 Å for *oP10-β*-CrB₄, respectively. As a result, hexagonal prism channels are formed in [100] direction, and hosted by zig-zag Cr chains with more uniform Cr-Cr separations 2.807 Å and 3.200 Å for *mP10-α*-CrB₄, 2.955 Å and 2.965 Å for *mP10-β*-CrB₄, and 3.172 Å for *oP10-β*-CrB₄. The zig-zag motif of Cr atoms in HP phases induces more close-packed stacking than the ground-state *oP10-α*-CrB₄, similar arrangement has also be found in VB₄ with relatively larger vanadium atom radius.³⁴

The calculated lattice parameters for CrB₄ and FeB₄ at ambient pressure are listed in Table 1. Calculated total energy relative to *Pnmm* structure is given for comparison. Our calculated equilibrium lattice constants agree well with the previous results within the error of 2.2%.^{8, 9, 17} The dynamic stabilities of new proposed HP phases for CrB₄ and FeB₄ are validated by calculating the phonon spectra (as shown in Fig. S3). The absence of imaginary phonon frequencies throughout the Brillouin Zone, except for *oP10-β*-CrB₄, indicates

Table 1 Calculated equilibrium lattice parameters *a*, *b*, and *c* (Å), β (deg), and relative total energy ΔE (eV/atom) of high-pressure phases in comparison with *Pnmm* phase

	S.G.	<i>a</i>	<i>b</i>	<i>c</i>	β	ΔE	Ref.
<i>oP10-α</i> -CrB ₄	<i>Pnmm</i>	4.714	5.466	2.848		0	
		4.7452(3)	5.4764(3)	2.8662(2)			Exp. ⁸
		4.7247	5.4756	2.8474			Theo. ⁸
<i>mP10-α</i> -CrB ₄	<i>P2/m</i>	5.333	2.826	4.882	103.208	0.181	
<i>mP10-β</i> -CrB ₄	<i>Pm</i>	5.262	2.886	4.694	82.973	0.295	
<i>oP10-β</i> -CrB ₄	<i>Pmma</i>	5.530	2.743	4.611		0.419	
<i>oP10-FeB₄</i>	<i>Pnmm</i>	4.476	5.250	3.015		0	
		4.5786(3)	5.2981(3)	2.9991(8)			Exp. ⁹
		4.521	5.284	3.006			Theo. ¹⁷
<i>tI40-FeB₄</i>	<i>I4₁/acd</i>	5.115		10.201		0.094	
		4.84		9.73			Theo. ²⁷
		5.136		10.242			Theo. ²⁸
<i>cP20-FeB₄</i>	<i>P2₁3</i>	5.093				0.202	

their dynamical stability at 0 K and zero pressure. For *oP10-β*-CrB₄, imaginary frequency is found in the Brillouin Zone at zero pressure (see Fig. S3(c)). At pressure above 294 GPa, however, all of phonon frequencies become positive (Fig. S3(d)), indicating the dynamical stability under compression.

Elastic constants of a crystal describe its response to an applied stress or the stress required to maintain a given deformation, which is directly related to elastic stability and mechanical properties. The satisfaction of the Born-Huang stability criteria³⁵ was firstly examined by their elastic constants, showing the mechanical stability

Table 2 Calculated elastic constants, *C_{ij}* (GPa), bulk moduli, *B* (GPa), shear moduli, *G* (GPa), Young's moduli, *E* (GPa), *G/B* ratio, Poisson's ratio ν and Vicker's hardness, *H_v* (GPa) at ambient pressure, compared with available experimental and theoretical results.

	<i>C₁₁</i>	<i>C₂₂</i>	<i>C₃₃</i>	<i>C₄₄</i>	<i>C₅₅</i>	<i>C₆₆</i>	<i>C₁₂</i>	<i>C₁₃</i>	<i>C₂₃</i>	<i>B</i>	<i>G</i>	<i>E</i>	<i>B/G</i>	ν	<i>H_v</i>	Ref.
<i>oP10-α</i> -CrB ₄	616	887	419	241	280	257	101	150	139	290	250	583	1.16	0.17	39.5	
	554	880	473	254	282	250	65	107	95	265	261				48.0	Theo. ⁸
															23.3-26.1	Exp. ¹⁵
<i>mP10-α</i> -CrB ₄	592	490	477	186	225	224	125	179	173	273	192	467	1.42	0.22	25.7	
<i>mP10-β</i> -CrB ₄	580	486	535	105	184	179	106	136	125	259	170	418	1.52	0.23	21.7	
<i>oP10-β</i> -CrB ₄	510	509	576	222	205	177	41	190	117	251	202	478	1.24	0.18	31.6	
<i>oP10-FeB₄</i>	424	717	498	218	143	230	86	139	90	249	200	473	1.25	0.18	31.3	
	432.50	753.40	455.60	223.50	156.26	221.98	138.56	133.15	130.21	264.73	197.97	475.41		0.2	28.4	Theo. ⁴⁶
										252					~43	Exp. ⁹
<i>tI40-FeB₄</i>	808		831	208		200	43	60		308	264	616	1.17	0.17	40.6	
										311.5						
	637		614	313		255	188	122		305	278	639		0.15	47.4	Theo. ²⁸
<i>cP20-FeB₄</i>	410			40			241			297	55	155	5.40	0.41	–	

of all proposed phases here. The calculated individual elastic constants of considered phases are listed in Table 2 and SI. Among HP phases, *tI40*-FeB₄ shows large C_{11} (808 GPa) and C_{33} values (831 GPa), comparable with C_{11} of *c*-BN (820 GPa).³⁶ Nevertheless, C_{11} , C_{22} and C_{33} values of HP phases for CrB₄ are very close (varied from 477 GPa to 592 GPa) due to the similar atomic arrangements, comparable with that of *Pnma*-RuB₃ and *Pnma*-OsB₃.³⁷ Especially, *cP20*-FeB₄ shows the ionic nature with an unusual low C_{44} value, 40 GPa, close to that of the half-Heusler insulator LiMgP.³⁸

The calculated bulk modulus (B), shear modulus (G), Young's modulus (E), and Poisson's ratio (ν) are listed in Table 2. The largest B (308 GPa) and G (264 GPa) values for *tI40*-FeB₄ phase are greater than that of *oP10- α* -CrB₄ ($B = 290$ GPa, $G = 250$ GPa) and *oP10*-FeB₄ ($B = 249$ GPa, $G = 200$ GPa), close to that of WB₄ ($B = 304$ GPa).¹² For HP phases of CrB₄, however, all the bulk modulus are lower than that of *oP10- α* -CrB₄, and slightly decrease from 273 GPa of *mP10- α* -CrB₄, 259 GPa of *mP10- β* -CrB₄, to 251 GPa of *oP10- β* -CrB₄. Meanwhile, G shows largest value for *oP10- β* -CrB₄, 202 GPa and smallest value for *mP10- β* -CrB₄, 170 GPa. Among HP phases, *cP20*-FeB₄ has the lowest shear modulus (55 GPa), quite close to ionic SrO.³⁹ Hardness is an important parameter for potentially technological application. The calculated Vicker's

hardness for *tI40*-FeB₄ based on empirical formulation of Chen *et al.*⁴⁰ is 40.6 GPa, well consistent with previously theoretical results 47.4 GPa,²⁸ indicating a potential superhard material. The estimated Vicker's hardness of *oP10- α* -CrB₄ is 39.5 GPa, comparable to that of the B₄C (31.3~38.9 GPa),⁴¹ B₆O (38 GPa)⁴² and γ -B (50 GPa)⁴³. The estimated hardness of *mP10- α* -CrB₄, *mP10- β* -CrB₄, *oP10- β* -CrB₄ are 25.7 GPa, 21.7 GPa, and 31.6 GPa, respectively. Poisson's ratio, ν , is another important parameter to describe the directional degree of covalent bonds in a material.⁴⁴ With the exception of *cP20*-FeB₄ ($\nu = 0.41$), all of proposed phases have relatively low Poisson's ratio (0.17-0.23), indicating the possible directional covalent bonding. The ratio of B/G is correlated with the ductility of materials (the threshold is 1.75, brittle ($B/G < 1.75$) and ductile ($B/G > 1.75$) manners).⁴⁵ The B/G ratio of *cP20*-FeB₄ is 5.4, much higher than the critical value (1.75), indicating its great ductility. The B/G values of the other phases proposed here are between 1.16 and 1.52, indicating the brittle features. Young's modulus (E) is an important mechanical parameter to measure the stiffness of a solid material. To get a better understanding of direction oriented Young's modulus, a 3D representation and corresponding two dimensional (2D) projections of Young's modulus for HP CrB₄ phases are calculated as a function of the crystallographic direction³⁵ and presented in Fig. 5. The shape deviation from a sphere indicates the

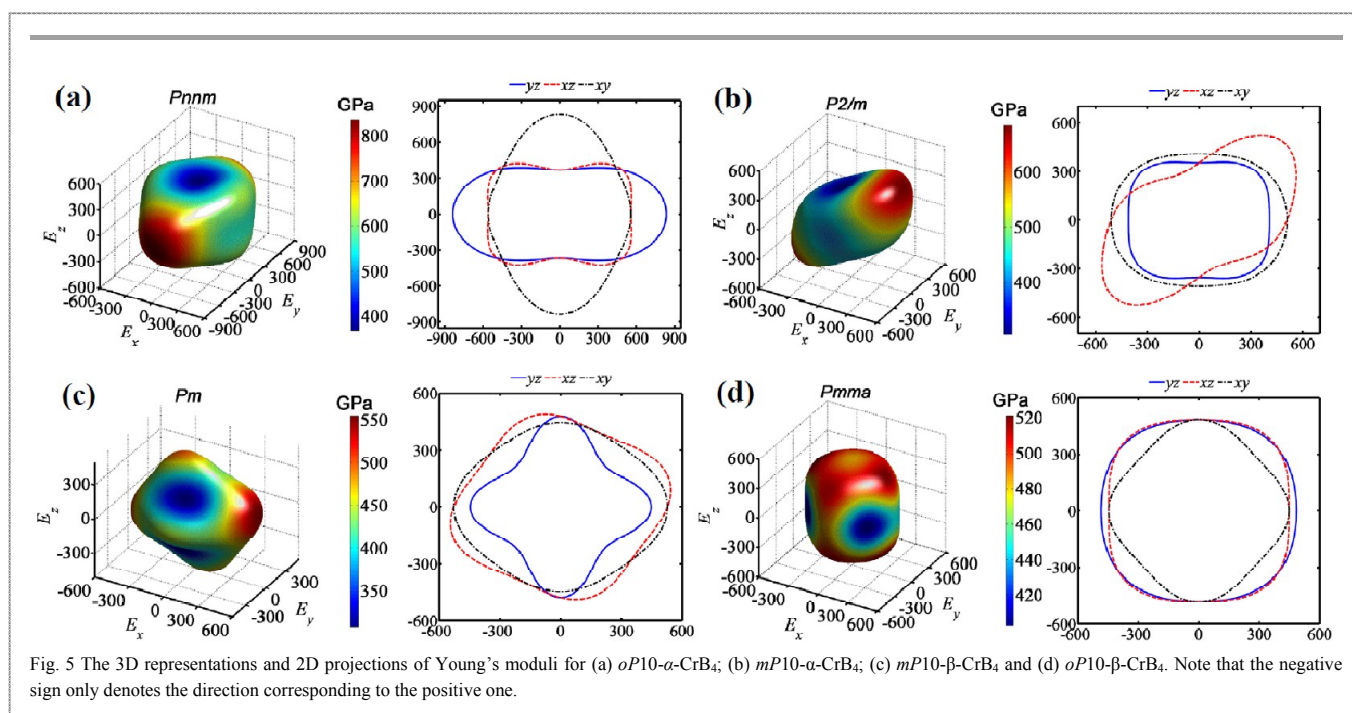


Fig. 5 The 3D representations and 2D projections of Young's moduli for (a) *oP10- α* -CrB₄; (b) *mP10- α* -CrB₄; (c) *mP10- β* -CrB₄ and (d) *oP10- β* -CrB₄. Note that the negative sign only denotes the direction corresponding to the positive one.

degree of anisotropy in the system. For $oP10-\alpha\text{-CrB}_4$, the 2D projections of Young's modulus in yz and xy planes exhibit small anisotropy, the lowest and highest Young's modulus values are found along $[001]$ and $[010]$ directions, respectively. The 2D projection of Young's modulus for $mP10-\alpha\text{-CrB}_4$ in xy plane is almost a regular ellipse, while in xz plane, the projection exhibits distinct anisotropy. For $mP10-\beta\text{-CrB}_4$, however, the anisotropy of Young's modulus is similar to $oP10-\alpha\text{-CrB}_4$ with the 2D projection of Young's modulus in yz plane showing larger anisotropy than the others. For $oP10-\beta\text{-CrB}_4$, the 2D projections of Young's modulus in yz and xz planes are close to regular circles, while the projection exhibits slight anisotropy in xy plane.

The band structure and density of states (DOS) for $tI40\text{-FeB}_4$ and $cP20\text{-FeB}_4$ are presented in Fig. 6. The Fermi level of $oP10\text{-FeB}_4$ catches the edge of the antibonding peak with a $E_F = 1.0$ states/(eV f.u.) and it was confirmed in experiment to be a superconductor.^{9,17} Intriguingly, both $tI40\text{-FeB}_4$ and $cP20\text{-FeB}_4$ exhibit the semiconducting feature with indirect band gap (shown in Fig. 6(a) and 6(c)). The calculated band gap of $tI40\text{-FeB}_4$, 1.63 eV, is in good agreement with previous theoretical reports, 1.34 eV by Jiang et al.²⁸ and 1.06 eV (at 50 GPa) by Kotmool et al.²⁷, while $cP20\text{-FeB}_4$ has a narrower band gap of 0.61 eV. As shown in Fig. 6(b) and 6(d), the bottom of valence band for both $tI40\text{-FeB}_4$ and $cP20\text{-FeB}_4$ are

contributed by B-2s and B-2p states and the top of valence bands are dominated by Fe-3d states. Significantly, the overlapping of B-2p states and Fe-3d states from -4.5 eV to 0 eV are relatively strong for both $tI40\text{-FeB}_4$ and $cP20\text{-FeB}_4$. It should be noted that the center of Fe-3d states are showing below Fermi level, which is different from other 3d metal borides, $oP10\text{-FeB}_4$, $oP10-\alpha\text{-CrB}_4$ and MnB_4 ¹¹, but similar to previous studied 5d metal borides, i.e., OsB_2 ,⁴⁷ ReB_2 ⁴⁸ and WB_3 ⁴⁹.

Fig. 7 represents the total and partial DOS for CrB_4 phases. Due to the close atomic stacking, the DOS profile of HP phases are quite close to each other, the valence band is dominated by B-2s states at low energy part, B-2p states in the middle range, and Cr-3d states at the higher energies. All CrB_4 phases exhibit the metallic feature due to the finite values at the Fermi level (E_F), which is mainly contributed by Cr-3d state. For $oP10-\beta\text{-CrB}_4$, the hybridization between B-2s and B-2p orbitals is relatively strong because of the increasing overlap in comparison with $mP10-\alpha\text{-CrB}_4$ and $mP10-\beta\text{-CrB}_4$, which may explain the higher shear modulus, Young's modulus and hardness (as shown in Table 2). Different from $tI40\text{-FeB}_4$ and $cP20\text{-FeB}_4$, Cr-3d states are more delocalized in a wide range from -8 eV to +8 eV with orbital center in the vicinity of 2 eV, indicating more Cr-Cr metallic feature and weaker Cr-B interactions.

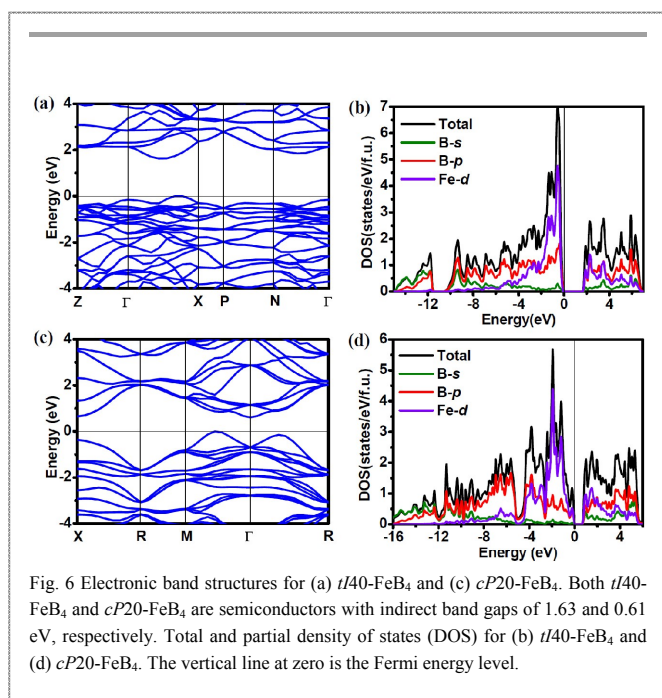


Fig. 6 Electronic band structures for (a) $tI40\text{-FeB}_4$ and (c) $cP20\text{-FeB}_4$. Both $tI40\text{-FeB}_4$ and $cP20\text{-FeB}_4$ are semiconductors with indirect band gaps of 1.63 and 0.61 eV, respectively. Total and partial density of states (DOS) for (b) $tI40\text{-FeB}_4$ and (d) $cP20\text{-FeB}_4$. The vertical line at zero is the Fermi energy level.

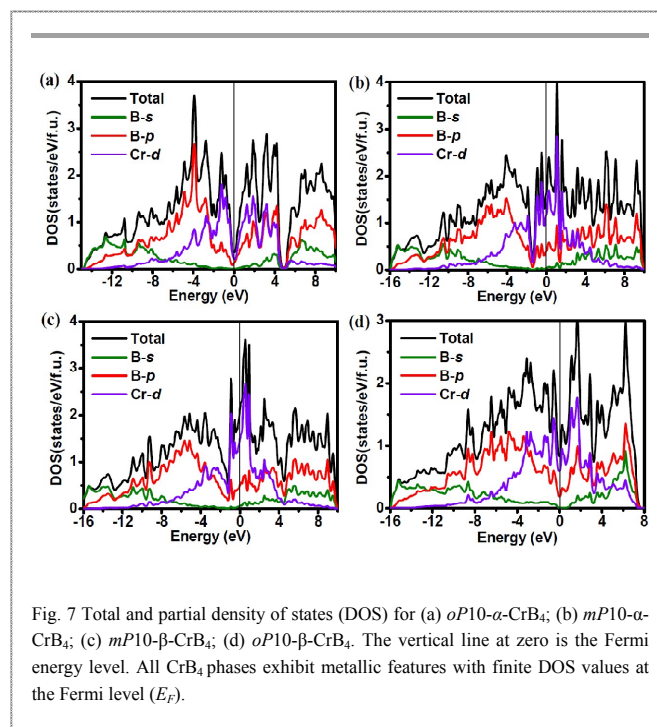
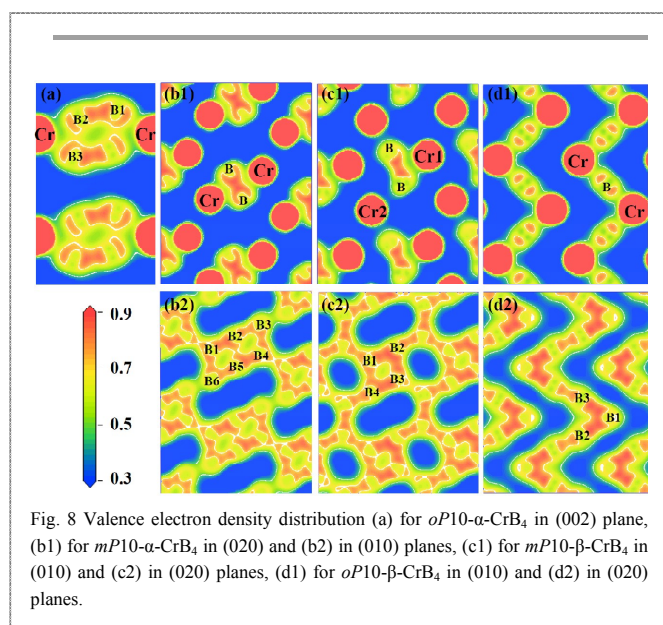


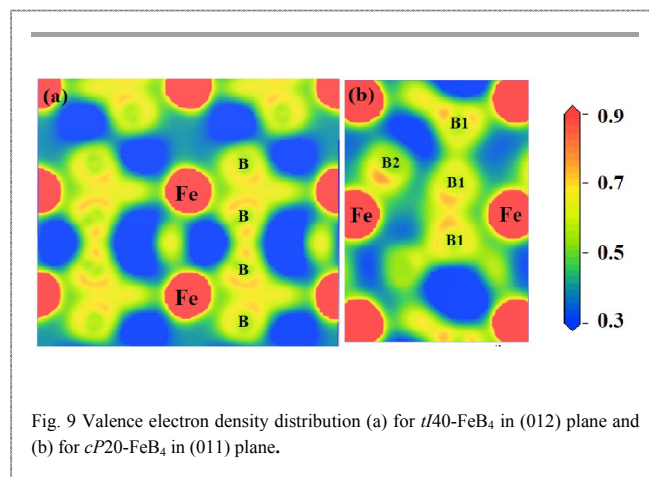
Fig. 7 Total and partial density of states (DOS) for (a) $oP10-\alpha\text{-CrB}_4$; (b) $mP10-\alpha\text{-CrB}_4$; (c) $mP10-\beta\text{-CrB}_4$; (d) $oP10-\beta\text{-CrB}_4$. The vertical line at zero is the Fermi energy level. All CrB_4 phases exhibit metallic features with finite DOS values at the Fermi level (E_F).

Fig. 8 and 9 represent the valence electron density distribution (VEDD), revealing the typical bonding characteristic for CrB_4 and FeB_4 phases. For CrB_4 phases, the high electron density regions are located in the middle of B atoms within planar boron sheets, indicating a strong nonpolar σ covalent bonding, furthermore, typical sp^2 hybridization can be observed between B1 and B4 atoms for $mP10-\alpha\text{-CrB}_4$ (in Fig. 8(b2)), B1 and B3 atoms for $mP10-\beta\text{-CrB}_4$ (in Fig. 8(c2)). However, in Cr-B layer, the valence electrons are more localized around B atoms due to the electronegativity difference, corresponding to a polar covalent bonding. The relative bond strength between boron atoms can be evaluated by the calculated Mulliken overlap populations (*MOP*) for CrB_4 phases. In $oP10-\alpha\text{-CrB}_4$, *MOP* is found to be 0.9 for B1-B2 bond, 0.63 for B2-B3 bond. The strong B1-B2 bond, nearly parallel to *b* axis, is responsible for its high incompressibility along this direction. For $mP10-\alpha\text{-CrB}_4$, *MOP* of the dumbbell B-B bond in Cr_2B_2 tetragon is 0.77. The strongest B-B bond is located in the B_6 rhomboid units, and *MOP* is 0.86 for B1-B2 and B4-B5 bonds, 0.68 for B3-B4 and B1-B6 bonds, 0.55 for B2-B3 and B5-B6 bonds, and 0.59 for B2-B5 bonds. For $mP10-\beta\text{-CrB}_4$, one of the two different Cr atoms and two dumbbell B atoms in Cr-B layer form CrB_2 triangle, and *MOP* value of the dumbbell B-B bond is 0.75. In B layer, each B_4 rhomboid is connected with the adjacent two hexatomic rings and two octatomic rings by sharing edges. The strongest B-B bond is located in the B_4 rhomboid, and *MOP* is 0.59 for B1-B2 bond, 0.68 for B2-B3 bond,



0.85 for B3-B4 bond, and 0.74 for B1-B4 bond. For $oP10-\beta\text{-CrB}_4$, Cr atoms and B atoms in Cr-B layer form zig-zag chains, and the electron density between Cr and B atoms exhibits local maximum values close to the B sites. In the B layer, each B_3 triangle is connected with the adjacent two ones by B-B bond in which the B atoms locate in the basic angle of the different triangles. The B-B bond connecting the B_3 triangles is relatively strong with a *MOP* of 0.85, greater than 0.78 for B1-B2 and B1-B3 bonds. The electron transfer from Cr to B atoms is found to be 1.28 *e* for $oP10-\alpha\text{-CrB}_4$, 1.16 *e* for $mP10-\alpha\text{-CrB}_4$, 1.11 *e* for Cr1 and 1.23 *e* for Cr2 in $mP10-\beta\text{-CrB}_4$, and 0.84 *e* in $oP10-\beta\text{-CrB}_4$, which is crucial for the stabilizations of boron networks in these structures.

Compared with the nonpolar σ covalent B-B bonding and polar covalent Cr-B bonding in CrB_4 , the Fe-B bonding in the FeB_4 exhibits more ionic characteristics, as demonstrated by the more electron transfer from Fe to B atoms (1.35 *e* in $tI40\text{-FeB}_4$ and 1.53 *e* in $cP20\text{-FeB}_4$) than Cr to B in CrB_4 . The ionic characteristics of the $tI40\text{-FeB}_4$ and $cP20\text{-FeB}_4$ may be attributed to the structure feature, resembling NaCl-type structures. For $tI40\text{-FeB}_4$, *MOP* of B-B bond in B_4 tetrahedron is 0.46, *MOP* of the B-B bond connecting the B_4 tetrahedrons is 0.71, and thus the hybridization in the three dimensional B network is mainly sp^3 hybridization. For $cP20\text{-FeB}_4$, *MOP* of B1-B1 bonds in B_3 equilateral triangle is 0.56, of the B1-B2 bonds connecting the B_3 equilateral triangle is 0.65, and the sp^3 type of hybridization is similar to that in $tI40\text{-FeB}_4$, due to the similar 3D boron network.



IV. Conclusions

In conclusion, we have extensively explored the high pressure phases of CrB₄ and FeB₄ using the particle swarm optimization technique in combination with first principles calculations. The phase transition from *oP10-α*-CrB₄ into *mP10-α*-CrB₄ at 196 GPa, into *mP10-β*-CrB₄ at 261 GPa and into *oP10-β*-CrB₄ at 294 GPa, is reported here for the first time. Meanwhile, *oP10*-FeB₄ transforms into *tI40*-FeB₄ at 48 GPa and into *cP20*-FeB₄ at 231 GPa. In particular, the *cP20*-FeB₄ is found to be more energetically preferable to the previously proposed *Im* $\bar{3}m$ phase in the pressure ranges of 231 GPa to at least 700 GPa. The phonon dispersion and elastic constants calculations have demonstrated the dynamical and mechanical stabilities of the proposed high-pressure phases for CrB₄ and FeB₄. *tI40*-FeB₄ and *cP20*-FeB₄ exhibit semiconducting feature, while *mP10-α*-CrB₄, *mP10-β*-CrB₄ and *oP10-β*-CrB₄ are metallic. Further, analysis of electronic structure reveals the high directional covalent bonding in these phases. Mechanical property calculations indicate that *tI40*-FeB₄ is a potential superhard material and *mP10-α*-CrB₄, *mP10-β*-CrB₄ and *oP10-β*-CrB₄ can be classified into hard materials. Our predictions may stimulate further researches in both experiment and theory.

Acknowledgements

This work was supported by National Natural Science Foundation of China (NSFC) under Grants No. 51201148 and U1530402. L. Wu thanks the foundation of Hebei Province Education Department under Grant No. QN2014114 and the Autonomic Research Project of Yanshan University under Grant No. 13LGB007. Z. Li thanks Hebei Natural Science Foundation (No. B2015203096) and the Autonomic Research Project of Yanshan University under Grant No. 14LGA017.

References

- V. V. Brazhkin, A. G. Lyapin and R. J. Hemley, *Philos. Mag. A*, 2002, **82**, 231-253.
- R. B. Kaner, J. J. Gilman and S. H. Tolbert, *Science*, 2005, **308**, 1268-1269.
- H.-Y. Chung, M. B. Weinberger, J. B. Levine, A. Kavner, J.-M. Yang, S. H. Tolbert and R. B. Kaner, *Science*, 2007, **316**, 436-439.
- R. W. Cumberland, M. B. Weinberger, J. J. Gilman, S. M. Clark, S. H. Tolbert and R. B. Kaner, *JACS*, 2005, **127**, 7264-7265.
- M. Hebbache, L. Stuparević and D. Živković, *Solid state commun.*, 2006, **139**, 227-231.
- X. Hao, Y. Xu, Z. Wu, D. Zhou, X. Liu, X. Cao and J. Meng, *Phys. Rev. B*, 2006, **74**, 224112.
- H. Gou, L. Hou, J. Zhang, H. Li, G. Sun and F. Gao, *Appl. Phys. Lett.*, 2006, **88**, 1904.
- H. Niu, J. Wang, X.-Q. Chen, D. Li, Y. Li, P. Lazar, R. Podloucky and A. N. Kolmogorov, *Phys. Rev. B*, 2012, **85**, 144116.
- H. Gou, N. Dubrovinskaia, E. Bykova, A. A. Tsirlin, D. Kasinathan, W. Schnelle, A. Richter, M. Merlini, M. Hanfland and A. M. Abakumov, *Phys. Rev. Lett.*, 2013, **111**, 157002.
- H. Gou, A. A. Tsirlin, E. Bykova, A. M. Abakumov, G. Van Tendeloo, A. Richter, S. V. Ovsyannikov, A. V. Kurnosov, D. M. Trots and Z. Konôpková, *Phys. Rev. B*, 2014, **89**, 064108.
- A. Knappschneider, C. Litterscheid, N. C. George, J. Brgoch, N. Wagner, J. Beck, J. A. Kurzman, R. Seshadri and B. Albert, *Angew. Chem. Int. Ed.*, 2014, **53**, 1684-1688.
- Q. Gu, G. Krauss and W. Steurer, *Adv. Mater.*, 2008, **20**, 3620-3626.
- I. Zeiringer, P. Rogl, A. Grytsiv, J. Polt, E. Bauer and G. Giester, *J. Phase Equilib. Diff.*, 2014, **35**, 384-395.
- A. T. Lech, C. L. Turner, R. Mohammadi, S. H. Tolbert and R. B. Kaner, *PNAS*, 2015, **112**, 3223-3228.
- A. Knappschneider, C. Litterscheid, D. Dzivenko, J. A. Kurzman, R. Seshadri, N. Wagner, J. Beck, R. Riedel and B. Albert, *Inorg. Chem.*, 2013, **52**, 540-542.
- A. Knappschneider, C. Litterscheid, J. Kurzman, R. Seshadri and B. Albert, *Inorg. Chem.*, 2011, **50**, 10540-10542.
- A. N. Kolmogorov, S. Shah, E. R. Margine, A. F. Bialon, T. Hammerschmidt and R. Drautz, *Phys. Rev. Lett.*, 2010, **105**, 217003.
- A. Knappschneider, C. Litterscheid, J. Brgoch, N. C. George, S. Henke, A. K. Cheetham, J. G. Hu, R. Seshadri and B. Albert, *Chem. Eur. J.*, 2015, **21**, 8177-8181.
- W. Zhang, A. R. Oganov, A. F. Goncharov, Q. Zhu, S. E. Boulfelfel, A. O. Lyakhov, E. Stavrou, M. Somayazulu, V. B. Prakapenka and Z. Konôpková, *Science*, 2013, **342**, 1502-1505.
- J. B. Neaton and N. W. Ashcroft, *Nature*, 1999, **400**, 141-144.
- Y. Ma, M. Eremets, A. R. Oganov, Y. Xie, I. Trojan, S. Medvedev, A. O. Lyakhov, M. Valle and V. Prakapenka, *Nature*, 2009, **458**, 182-185.
- S. M. Woodley and R. Catlow, *Nature Mater.*, 2008, **7**, 937-946.
- G. Hautier, C. C. Fischer, A. Jain, T. Mueller and G. Ceder, *Chem. Mater.*, 2010, **22**, 3762-3767.
- G. Hautier, A. Jain and S. P. Ong, *J. Mater. Sci.*, 2012, **47**, 7317-7340.
- Y. Wang, J. Lv, L. Zhu and Y. Ma, *Phys. Rev. B*, 2010, **82**, 094116.
- Y. Wang, J. Lv, L. Zhu and Y. Ma, *Comput. Phys. Commun.*, 2012, **183**, 2063-2070.
- K. Kotmool, T. Kaewmaraya, S. Chakraborty, J. Anversa, T. Bovornatanaraks, W. Luo, H. Gou, P. C. Piquini, T. W. Kang and H.-k. Mao, *PNAS*, 2014, **111**, 17050-17053.
- X. Jiang and J. Zhao, *RSC Adv.*, 2015, **5**, 48012-48023.
- S. J. Clark, M. D. Segall, C. J. Pickard, P. J. Hasnip, M. I. J. Probert, K. Refson and M. C. Payne, *Z. Kristallogr.*, 2005, **220**, 567-570.
- J. P. Perdew, K. Burke and M. Ernzerhof, *Phys. Rev. Lett.*, 1996, **77**, 3865.
- R. Hill, *Proc. Phys. Soc. A*, 1952, **65**, 349.
- K. Momma and F. Izumi, *J. Appl. Crystallogr.*, 2011, **44**, 1272-1276.
- M. Atoji and W. N. Lipscomb, *Acta Cryst.*, 1953, **6**, 547-550.
- L. Wu, B. Wan, Y. Zhao, Y. Zhang, H. Liu, Y. Wang, J. Zhang and H. Gou, *J. Phys. Chem. C*, 2015, **119**, 21649-21657.
- J. F. Nye, *Physical properties of crystals*, Oxford university press, 1985.
- M. Grimsditch, E. S. Zouboulis and A. Polian, *J. Appl. Phys.*, 1994, **76**, 832-834.
- Y. Wang, T. Yao, L.-M. Wang, J. Yao, H. Li, J. Zhang and H. Gou, *Dalton Trans.*, 2013, **42**, 7041-7050.
- A. Roy, J. W. Bennett, K. M. Rabe and D. Vanderbilt, *Phys. Rev. Lett.*, 2012, **109**, 037602.
- T. Tsuchiya and K. Kawamura, *J. Chem. Phys.*, 2001, **114**, 10086-10093.
- X.-Q. Chen, H. Niu, D. Li and Y. Li, *Intermetallics*, 2011, **19**, 1275-1281.
- S. Grasso, C. Hu, O. Vasylykiv, T. S. Suzuki, S. Guo, T. Nishimura and Y. Sakka, *Scripta Mater.*, 2011, **64**, 256-259.

ARTICLE

Journal Name

- 42 H. F. Rizzo, W. C. Simmons and H. O. Bielsstein, *J. Electrochem. Soc.*, 1962, **109**, 1079-1082.
- 43 V. L. Solozhenko, O. O. Kurakevych and A. R. Oganov, *J. Superhard Mater.*, 2008, **30**, 428-429.
- 44 J. Haines, J. M. Leger and G. Bocquillon, *Annu. Rev. Mater. Res.*, 2001, **31**, 1-23.
- 45 S. F. Pugh, *Philos. Mag.*, 1954, **45**, 823-843.
- 46 M. Zhang, M. Lu, Y. Du, L. Gao, C. Lu and H. Liu, *J. Chem. Phys.*, 2014, **140**, 174505.
- 47 S. Chiodo, H. J. Gotsis, N. Russo and E. Sicilia, *Chem. Phys. Lett.*, 2006, **425**, 311-314.
- 48 Y. X. Wang, *Appl. Phys. Lett.*, 2007, **91**, 1904.
- 49 Y. Liang, Z. Fu, X. Yuan, S. Wang, Z. Zhong and W. Zhang, *EPL*, 2012, **98**, 66004.